Chemical Engineering Journal 543 (2026) 178373

Contents lists available at ScienceDirect

Chemical Engineering Journal

journal homepage: www.elsevier.com/locate/cej

Quantitative control over Lorentz effects in magneto-electrochemistry

Haihui Joy Jiang [a,b], Lais C. Brazaca [a,c], Thomas C. Underwood [a,d], Ekaterina V. Skorb [a,e], Mohamed K. Abd El-Rahman [a,f], Craig A. Mascarenhas [a,g], William T. McLeod [h], Gigi Ni [a], Brian Medrano [a], Lukas Emge [a], Lee Belding [a], Albert S.Y. Wong [a], David M. Wilmouth [a,g], Dimitar D. Sasselov [b], James G. Anderson [a,g], Jeffrey G. Bell [a,h,*], George M. Whitesides [a,**]

[a] Department of Chemistry and Chemical Biology, Harvard University, Cambridge, MA, 02138, USA
[b] Department of Astronomy, Harvard University, Cambridge, MA, 02138, USA
[c] São Carlos Institute of Chemistry, University of São Paulo, São Carlos, SP, 13566-590, Brazil
[d] Department of Aerospace Engineering and Engineering Mechanics, The University of Texas at Austin, Austin, TX, 78705, USA
[e] ITMO University, St. Petersburg, 191002, Russian Federation
[f] Department of Analytical Chemistry, Faculty of Pharmacy, Cairo University, Kasr-El Ani Street, Cairo, 11562, Egypt
[g] Harvard John A. Paulson School of Engineering and Applied Sciences, Harvard University, Cambridge, MA, 02138, USA
[h] Department of Chemistry, College of Arts and Sciences, Washington State University, Pullman, WA, 99164, USA

ARTICLE INFO

Keywords:
Lorentz force
Magneto-hydrodynamics
Mass transport
Fluid dynamics
Electro-synthesis

ABSTRACT

Overcoming mass transport limitations is a central challenge that constrains the efficiency of diverse electrochemical technologies, from industrial electrosynthesis to energy storage. Here, we establish a design framework for the quantitative, predictive control of solution-phase fluid dynamics using Lorentz forces, transforming this phenomenon from a physical curiosity into a robust chemical engineering tool. Using the electrochemical oxidation of iodide as a tracer-free model system, we directly visualize and deconstruct the parameters governing magneto-hydrodynamic convection. We provide quantitative correlations linking key chemical (reactant concentration, electrolyte viscosity) and physical (applied potential, magnetic field strength) parameters to the resulting fluidic motion. This analysis reveals a fundamental insight: both the electric and magnetic components of the Lorentz force create observable, controllable transport effects extending millimeters from the electrode surface, with both force components quantified on the same order of magnitude (e.g., 10^1–10^2 N/m^3). This work provides a non-mechanical strategy to rationally engineer fluid dynamics in electrochemical reactors, opening a clear pathway to predictably enhance rates in diffusion-limited electrocatalysis (e.g., increasing currents by up to 100% without mechanical stirring) and homogenize interfacial processes in batteries.

1. Introduction

The efficiency of critical electrochemical technologies, from industrial-scale electrosynthesis to modern energy storage, is often constrained by the slow, diffusion-limited mass transport of ions and reactants to electrode surfaces [1,2]. While mechanical stirring is a common solution, it is impractical in sealed devices and lacks precision for controlling interfacial phenomena. An alternative, non-mechanical strategy is to use magnetic fields to induce fluid flow (magneto-hydrodynamics) via the Lorentz force [3,4]. Studies have shown that this effect can influence electrochemical processes such as metal electrodeposition, battery performance, hydrogen production, and CO_2 reduction [5–11]. However, despite these successes, the field has largely remained a qualitative curiosity. The fundamental transport mechanisms remain poorly understood, and a design framework is missing, preventing the *predictive* and *quantitative* control of fluid motion in response to chemical and physical parameters.

Fundamentally, the Lorentz effect is a physical phenomenon used in a variety of established technologies (e.g., electrical generators, electric motors, and Hall effect imaging) [12–14]. The effect has also been used in microfluidics to either control fluid flow or allow for sufficient mixing, making important contributions to miniaturized biomedical devices [15]. Based on mathematical and physical principles, the Lorentz force can be described from a single-particle perspective, in which a charged

* Correspondence to: J.G. Bell, Department of Chemistry, College of Arts and Sciences, Washington State University, Pullman, WA, 99164, USA.
** Corresponding author.
E-mail addresses: jeffrey.g.bell@wsu.edu (J.G. Bell), gwhitesides@gmwgroup.harvard.edu (G.M. Whitesides).

https://doi.org/10.1016/j.cej.2026.178373
Received 10 February 2026; Received in revised form 28 May 2026; Accepted 12 June 2026
Available online 13 June 2026

particle moving within electric and magnetic fields experiences a Lorentz force ($\vec{F}_L$), which is the sum of the electric component ($\vec{F}_E$) and the magnetic component ($\vec{F}_m$). The electric force component depends on the net charges (q) and the electric field ($\vec{E}$). In the case of quantifying Lorentz forces exerted on individual particles, the magnetic component depends on q, the velocity of net charges ($\vec{v}$) and the magnetic field ($\vec{B}$), as shown in Eqs. (1)–(3),

$$\vec{F}_L = \vec{F}_E + \vec{F}_m \quad (1)$$

$$\vec{F}_E = q\vec{E} \quad (2)$$

$$\vec{F}_m = q\vec{v} \times \vec{B} \quad (3)$$

While White, Coey, and co-workers conducted early studies of Lorentz effects in electrochemical systems [4,16], engineering models used to date often rely on a simplified interpretation ($\vec{F}_L \approx \vec{F}_m = q\vec{v} \times \vec{B}$) that treats $\vec{F}_E$ as negligible in the bulk [4,16,17]. While these diffusion-only or zero-migration approximations can predict current responses, they do not capture the full scope of forces driving bulk convection. This distinction is particularly important when the observable is not only current, but also solution based fluidic motion and spatial distribution of reaction products. In operating electrochemical cells, the ohmic potential drop generates a bulk electric field (i.e., $\vec{F}_E \neq 0$) whose magnitude and topology depend on cell geometry, current distribution, and electrolyte resistance. Rather than replacing established diffusion-migration models, the present work focuses on experimentally quantifying when and how $\vec{F}_E$ and $\vec{F}_m$ become observable in macroscopic solution volumes, offering a new dimension for rational electrochemical device engineering.

In plasma (ionic gas) systems, the electric field could be completely shielded in the bulk with low currents (~mA) [18], though as the current increases (to ~A), the electric field penetrates throughout and is needed to support the current flow [19]. It is unclear if there is a critical threshold for ionic current in electrochemical systems to observe the effect of $\vec{F}_E$, and how to precisely control ionic motion in liquid electrolytes by applying a magnetic field. Moreover, how Lorentz-induced fluidic motion influences reactions on reactive surfaces (e.g., on electrocatalysts), and how chemical (e.g., consumption or passivation) and physical (e.g., transport) processes couple between the liquid electrolyte and the liquid-electrode interface remains largely unknown. These are important questions to address for utilizing magnetism in electrochemistry, for applications such as electrocatalysis [17,20,21], lithium-based batteries [7], supercapacitors [22], microfluidic devices [23], and electrodeposition processes [24,25].

To establish a quantitative control framework for Lorentz forces, we designed a model system (Eqs. (4)–(7) and Fig. 1A) that involves the oxidation of iodide (I^-) forming a colored product, triiodide (I_3^-; charge balanced with a cation), at the surface of a platinum electrode [26]. Iodide salts are electro-active, and when a voltage is applied, I^- is oxidized to generate I_2 (Eq. (5)), which is insoluble in water but rapidly combines with solution-based I^- to form a soluble product, I_3^- (Eq. (6)) [27,28]. The triiodide complex appears brown and can be monitored using optical video analysis. Solvated triiodide complexes have a higher density than an aqueous solution of iodide salt (e.g., ρ([NaI] = 500 mM) = 1.060 g/mL), enabling in-situ tracking of fluidic motions in the bulk solution over time without over-accumulation of products at the electrode surface.

$$\text{Net ionic equation}: 3I^- + 2H_2O \rightarrow I_3^- + 2OH^- + H_2 \quad (4)$$

$$\text{At the anode}: 2I^- \rightarrow I_2 + 2e^- \quad (5)$$

$$I_2 + I^- \rightarrow I_3^- \ (\text{brown} - \text{colored}) \quad (6)$$

$$\text{At the cathode}: 2H_2O + 2e^- \rightarrow H_2 + 2OH^- \quad (7)$$

The simplicity of this electrochemical system offers a high level of control to obtain quantitative correlations between experimental parameters and Lorentz-induced fluidic motions. While previous work has utilized scanning electrochemical microscopy to probe current flux with micro-scale resolution [29], or used colored redox products for qualitative visualization of fluidic flow in thin layers [16], our work directly visualizes the angular velocity of the fluid in a macroscopic volume.

The goal of this study is to provide, and validate, an experimental framework that overcomes bottlenecks related to predicting and quantifying the effect of magnetic fields on diverse electrochemical

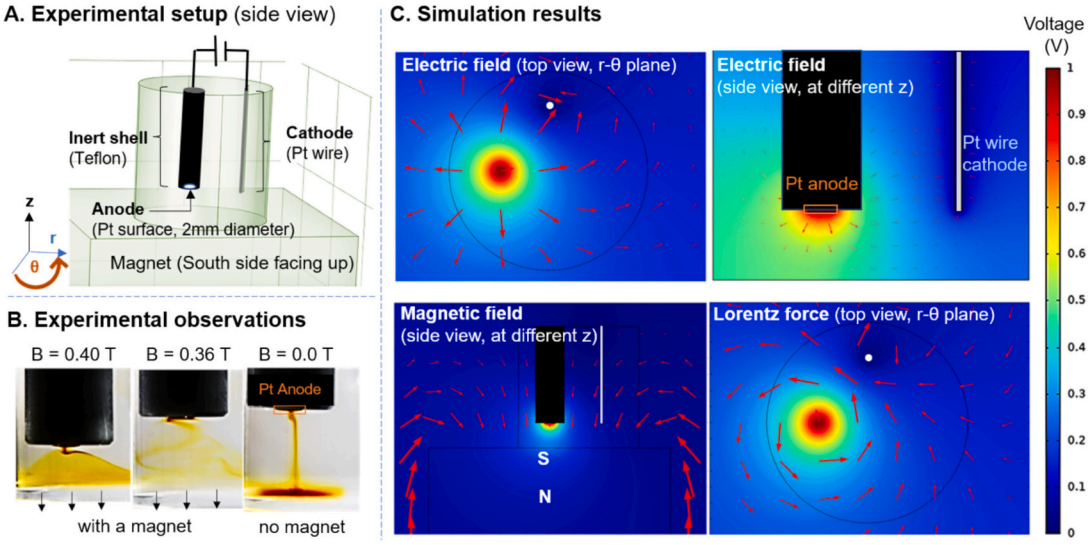

Fig. 1. A) Schematic representation of the experimental setup to investigate Lorentz effects on an operating electrochemical cell. A cylindrical coordinate system (r, θ, z) is used throughout this work. B) Experimental snapshots near the Pt anode, capturing the electrochemical oxidation of NaI (500 mM) in the absence (B = 0 T) vs. in the presence of a magnetic field (B = 0.40 T at the anode surface). C) COMSOL Multiphysics simulations of the applied electrical field assuming a uniform ion distribution that is static, magnetic field (when the south side of the magnet is facing up), and the resulting (initial, approximated) Lorentz forces in our system, assuming the initial ionic motion is in the same direction as the electric field. All the vectors shown in the images are scaled logarithmically.

parameters and their associated electrochemical outputs. Crucially, without adding auxiliary chemicals, this model system enables in-situ tracking of fluid dynamics, correlating Lorentz effects to individual experimental parameters (including the strength of an applied magnetic field, the magnitude of an applied voltage, the concentration of reactants, and viscosity of the electrolyte) to establish a generalized design framework applicable to diverse electrochemical systems.

2. Results

This study used NaI as an example of a starting material, which formed NaI_3 as an example of a colored oxidation product, and as the major product across the range of voltages tested (SI Sec.3, product speciation). In addition to sodium, other electrochemically inert cations, such as NH_4^+, Li^+, K^+, Mg^{2+} and Ca^{2+}, could be used to tune surface capacitance and solution resistance, which are discussed in detail in SI Sec. 6 and Figs. S8–9.

Fig. 1A shows a schematic representation of our experimental setup to investigate Lorentz effects. An asymmetric layout was selected for this study to break field symmetry, isolate force components, and optimize tracer visualization. A comprehensive fundamental and practical justification for this geometric configuration is provided in SI Sec. 1. We first examine the electro-oxidation of an iodide salt (NaI) in the presence and absence of an applied magnetic field. In the absence of an external magnetic field, the triiodide complex (NaI_3) desorbs from the electrode surface as a uniform, thin stream (Fig. 1B, left; Video S1 left). In the presence of an external magnetic field, however, the triiodide complex adopts a spiral pattern as it falls towards the bottom of the cell (Fig. 1B, right; Video S1 right). The transport of the product complex downwards is driven by the resulting force based on gravity and buoyancy effects within the electrolyte. Finite element analysis-based simulations enable the visualization of the applied electric and magnetic fields within the electrolytic cell before ionic rearrangement (Fig. 1C).

In solution-based electrochemical systems, as in many hydrodynamic systems, it is convenient to analyze forces on a per-volume (V) basis. This represents the total force as the sum of contributions from all species integrated over a unit volume,

$$\frac{\vec{F_L}}{V} = \frac{\vec{F_E}}{V} + \frac{\vec{F_m}}{V} \tag{8}$$

$$\frac{\vec{F_E}}{V} = \frac{q}{V}\vec{E} \tag{9}$$

$$\frac{\vec{F_m}}{V} = \frac{I}{A}\hat{n} \times \vec{B} = \vec{J} \times \vec{B} \tag{10}$$

where I is the ionic current, $\hat{n}$ is the unit vector of the current direction, A represents the surface area that an ionic current is flowing through, $\frac{q}{V}$ is the spatial charge density (considering all species present) or the concentration of net (unpaired) charged ions within the unit volume, and $\vec{J}$ is the current density.

Using Eqs. 8–10, the simulated fields were used to demonstrate the influence of Lorentz forces (Fig. 1C), showing that charged particles will adopt a circular trajectory around the electrode surface, agreeing with our experimental observations. Since the ionic current must be equal and non-zero everywhere in an electrochemical system, moving ions at various distances from the electrode surface all experience Lorentz forces, though to different extent and in different directions. The Lorentz force on ions drives bulk hydrodynamic transport through collisions with neutral molecules within the electrolyte, ultimately driving the rotational behavior observed in our system.

Having an active ionic current means there is continuous motion of net-charged species throughout the electrochemical cell—predominantly unpaired cations near the anode, and unpaired anions near the cathode. At the Pt anode, as the oxidation reaction occurs (which consumes anions), there is a local excess of cations (e.g., Na^+, $\frac{q}{V} > 0$, as a result of the oxidation reaction) moving in the direction of $\vec{E}$, which has a strong radial component pointing outwards (in the r-direction) from the anode to the cathode. In the r-θ (horizontal) plane, the radial component of $\vec{I}$ is perpendicular to $\vec{B}$ that is primarily pointing in the z- (vertical) direction. As the Lorentz force acts on the moving charged ions (i.e., the ionic current), this results in an angular velocity (in θ-direction) and fluidic rotations. With the south-pole of the magnet facing towards our electrochemical cell (i.e., magnetic field lines point downwards, in the negative z-direction), we observe counterclockwise fluidic rotation around the anode (where cations are in excess, $\frac{q}{V} > 0$) and clockwise around the cathode (where anions are in excess, $\frac{q}{V} < 0$). These observations are consistent with the right-hand rule of electromagnetism, and they agree with the results of the simulation. The geometry and the position of electrodes define the $\vec{E}$, and the space filled by the electrolyte defines boundary conditions of $\vec{J}$. These factors all influence Lorentz forces and the resulting fluidic motion throughout the electrolyte.

Fig. 2A shows experimental observations of fluidic rotations and methods of analysis. In the absence of a magnetic field, as a control scenario, the brown-colored NaI_3 desorbs from the electrode stream off the electrode and pools at the bottom of the cell, as the fluid is acted on solely by i) the electrical force, ii) gravity balanced with buoyancy, iii) multi-directional diffusion, and iv) fluidic drag. In the presence of a magnetic field (pointing downwards), the ionic current (e.g., with net charges distributed across the entire bulk electrolyte to sustain the current path) is acted upon by the Lorentz force, which leads to counterclockwise fluidic rotation around the anode and clockwise fluidic rotation around the cathode, both observed in the bulk (millimeters to centimeters away from the electrode surfaces). The increasing radial offset of ions as they move away from the anode is a result of the growing rotational speed as the ions experience higher field strengths. This rotation generates a centripetal acceleration that balances the radial outward motion, consistent with the dynamics of circular motion. These multi-physics features, including enhanced convection, are controllable via a surface mediated process together with externally tunable parameters. Using video analysis, we track the trajectory of NaI_3 (brown species) over time at 0.47 mm vertically away from the electrode surface, with the approximation that its motion in the r-θ (horizontal) plane follows the motion of the bulk fluid. These spatio-temporal patterns (kymographs) are constructed by extracting a fixed region from successive video frames and stacking them chronologically over time (Fig. 2A; SI Sec. 11). This method gives information on fluidic rotational frequency and rotational radius, which are used for quantifying Lorentz effects throughout this study.

Knowing that Lorentz forces can influence electrochemical systems, including driving convection in the bulk, improving mass transport in the diffusion layer, and enhancing electrochemical currents [11,20], we quantitatively correlate the global fluid dynamics with the resulting current and investigate the tunable parameters that control them systematically.

2.1. The effect of the applied voltage

Electrochemistry is highly reliant on an understanding of the influence of applied voltages on interfacial reactivity and processes. For example, standard redox potentials for a given chemical species govern the required voltage/potential (V) input necessary to result in oxidation/reduction processes to occur, leading to control over potential dependent processes and reactivity. Experimentally, deviations from theoretical standard reduction potentials are commonplace and are termed an overpotential (i.e., the additional potential needed experimentally to obtain reactivity). Minimization of overpotentials is one of

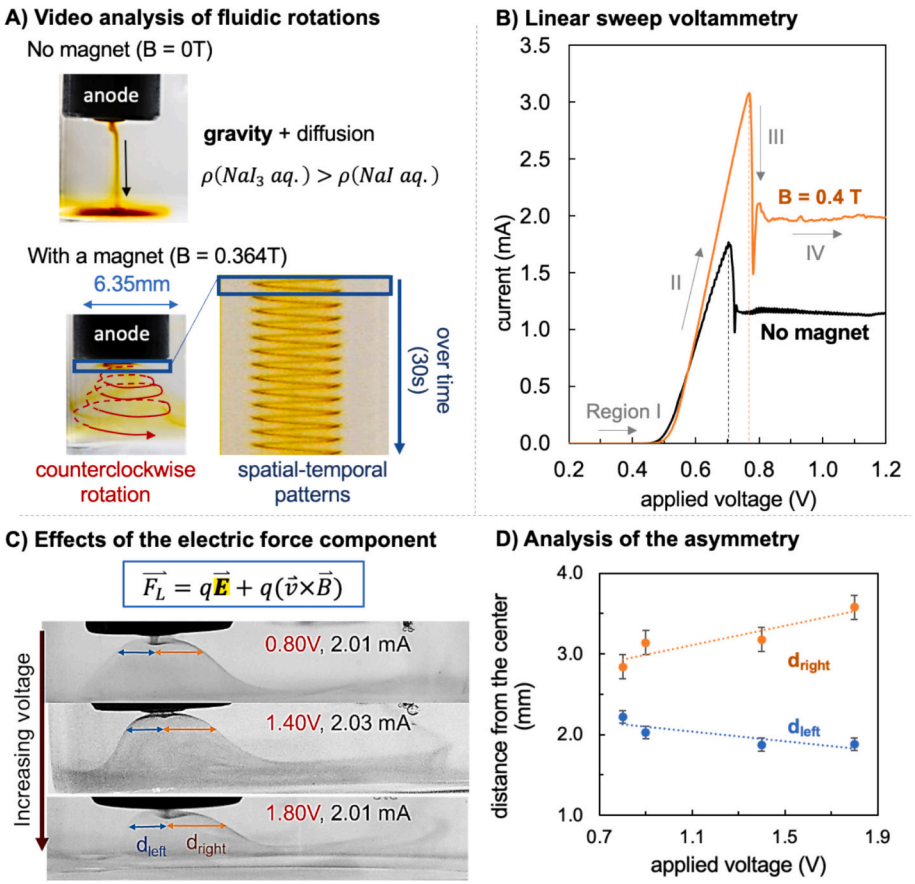

Fig. 2. Electrochemical reaction of aqueous NaI (500 mM): A) Experimental snapshots around the anode (with an applied voltage = 0.75 V vs. Ag/AgCl) showing fluidic rotations with an externally applied magnetic field. Spatio-temporal patterns were recorded for the analysis of rotational frequencies and radii. A falling stream of I_3^- (without rotations) was observed without an external magnet. B) Linear sweep voltammetry (scanned at 2 mV/s from 0.2 to 1.2 V vs. Ag/AgCl) shows four regions including (I) no reaction (II) reaction (III) passivation and (IV) with limiting current. C) Experimental snapshots showing the effect of increasing voltage at a constant current. D) Analysis of asymmetry of fluidic rotation relative to the center of rotation. Note that the counter electrode (i.e., cathode) is placed on the right-hand side of the anode. An externally applied magnetic field has a strength of B = 0.40 T at the position of the anode, unless specified.

the primary goals in energy storage and electrocatalytic applications and is directly linked to voltage efficiency. To select the range of voltage and current for quantifying Lorentz effects experimentally, we performed linear sweep voltammetry (LSV) at a scan rate of 2 mV/s, shown in Fig. 2B, in the presence and absence of an external magnet. There are four observable regions in the voltammogram: Region I) no reaction occurs when the applied voltage is below 0.45 V (vs. Ag/AgCl); Region II) oxidation occurs as iodide is oxidized into iodine (and subsequently triiodide) between 0.45 V and the peak (0.70 V when B = 0 T, or 0.78 V when B = 0.4 T). In the low-current regime (Region I/II), mass transport is not yet the limiting factor. While the magnetic field enhances convection, the current response here is primarily dictated by reaction kinetics and the specific overpotential, rather than bulk reactant concentration. Region III) passivation occurs (between 0.70 V and 0.72 V when B = 0 T, or between 0.78 V and 0.79 V when B = 0.4 T), as the insoluble I_2 accumulates, blocks active surface sites, and inhibits oxidation; Region IV) the current is limited when the passivation effect of I_2 balances with further oxidation of I_3^- at higher voltages. This current plateau is a unique feature of the iodide system that enables us to independently quantify $\vec{F_E}$ while keeping the current (and thus $\vec{F_m}$) constant.

In the presence of a magnetic field, we observe an enhanced current across all four regions from II to IV, above 0.6 V, indifferent to the specific electrochemical process occurring. Note that Lorentz effects are not limited to electrochemical processes that involve the formation of electrode-passivating species, as we observe similar effects when using different solvents (e.g., water-acetonitrile mixtures) in which the product is fully soluble (SI, Fig. S10). Additionally, the speciation of iodide oxidation products is studied in detail (SI Sec. 3).

To investigate the influence of the electric force component ($\vec{F_E}$), we selected the current-limiting region at high voltages and varied the electric field by varying the applied voltage from 0.8 to 1.8 V. Within this voltage range, this unique system has a constant current ($I = 2.02 \pm 0.01$ mA; thus a constant $\vec{F_m}$) under a fixed magnetic field (B = 0.40 T). Experimental snapshots in Fig. 2C (taken from amperometry experiments at a given potential) show asymmetrical effects of the applied *E*-field on fluidic motion, indicated by the dark-colored NaI_3 complex tilting towards the cathode (i.e., Pt wire is placed on the right). Quantitative asymmetrical analysis in Fig. 2D shows that rotational radius to the left (away from the cathode) decreases, while rotational radius to the right (towards the position of the cathode) increases, as the applied voltage increases. The increase in electric field causes an enhancement in rotational asymmetry that is beyond bulk body forces based on the flow of total current, which is kept constant within the experiments. Instead, our system demonstrates how applied potential and electrical forces can change transport trajectories of ions in the bulk electrolyte. These effects cannot be explained solely by the long-existing approximation in the literature that $\frac{\vec{F_L}}{V} \approx \frac{\vec{F_m}}{V} = \vec{J} \times \vec{B}$, which assumes $\vec{F_E} = 0$ in electrolytes [4,17,30]. By quantifying this interaction, this study demonstrates that the electric field is not only a background driving force for migration, but also a tunable lever for shaping fluid dynamics in 3D

space. It is worth noting that without the magnetic field, this horizontal displacement driven by $\vec{F_E}$ is less observable (Video S1) because the high local density of the product stream creates a gravitational force that dominates the vector sum, masking the electric force's contribution.

2.2. The effect of the magnetic field strength

An understanding of the magnetic field strength required to influence an electrochemical system (whether it is an interfacial or bulk solution process) is of paramount importance in the design of magneto-electrochemical systems and devices. For example, magnetic field strengths between 0.2 and 0.3 T were used to improve mass transport during the electrocatalytic reduction of CO_2 [11], whereas between 0.04 and 0.4 T was used to enhance water electrolysis [31,32]. Alternatively, mild magnetic fields (~0.03–0.07 T) were shown to influence the performance (i.e., cyclability, open-circuit voltage, rate-capability, dendrite formation, etc.) of aqueous Zn-bromide batteries when low-profile magnets were embedded into the battery housing [33]. Owing to the large variation in applied magnetic field strengths in electrochemical applications, we investigated the effect of B-field on fluidic rotations, as shown in Fig. 3. We performed experiments at a constant potential of 0.75 V (selected based on the position of peak current) with different strengths of *B*-field. At a given magnetic field (e.g., B = 0.40 T), we can quantify the magnetic component of the Lorentz force (Eq. (10)) based on the observed current measured at the electrode surface ($I = 1.98$ mA) at steady state (e.g., between 80 and 180 s since reaction started in this setup), and the proportion of current flowing in the r-θ direction (perpendicular to the magnetic field):

$$\frac{\vec{F_m}\,(1\ \mu m\ from\ the\ anode\ surface)}{V} = 0.075N \Big/ m^3$$

$$\frac{\vec{F_m}\,(bulk, 0.47mm\ below\ the\ anode\ surface)}{V} = 45\ N \Big/ m^3$$

As the surface of the anode is parallel to the surface of the magnet underneath, the electric field is mostly (>99.97%) parallel to the magnetic field at the anode surface, resulting in a negligible magnetic force (e.g., <0.1 N/m^3). In the bulk electrolyte and further away from the anode surface (e.g., 0.47 mm below and 1.56 mm to the side), over 90% of the electric field (and therefore the ionic current) is perpendicular to the magnetic field, where the magnetic component of the force reaches 45 N/m^3, quantified based on experimental observations. Details of the calculations are shown in SI Sec. 10.4 and Fig. S18–19. We analyzed the fluid dynamics within a representative probe volume ($r = 1.56$ mm and z = 0.466 mm) to demonstrate the quantitative tracking capabilities. However, because Lorentz effects propagate throughout the entire continuum of the cell (Video S1), this framework can be applied to characterize flow fields in any region of interest within a reactor. Experimental results suggest that, even without a significant magnitude of the Lorentz forces exerted on the electrode surface directly, Lorentz forces act on the bulk electrolyte driving fluidic convection which still influences electrochemical behavior.

As the applied B-field increases from 0.33 to 0.44 T, the magnetic component of the force increases. As a result, NaI_3 rotates with a smaller radius (decreased from 2.2 mm to 1.4 mm), at a higher frequency (increased from 0.24 Hz to 1.2 Hz), with higher centripetal acceleration (increased from 5 to 79 mm/s^2) and higher centripetal forces per volume (increased from 5 to 83N/m^3) (Fig. 3B). In the bulk solution along the z-axis (in the vertical direction), the angular velocity of the vortex (induced by Lorentz forces) increases as it gets closer to the magnet, where the magnetic field is the strongest. As $\frac{\vec{F_m}}{V}$ depend on both the current density and the magnetic field, systems with higher current densities (e.g., in batteries, fuel cells, and redox reactions with fast kinetics) require lower magnetic field strengths to observe Lorentz-induced fluidic motions.

Knowing the influence of $\vec{B}$, we further explore experimental parameters that control the magnitude of $\vec{I}$, which influences the q (net charges) term of both the electric force component and the magnetic force component of the Lorentz force. To evaluate how concentration and diffusivity are expected to influence this system, we consider the classical Cottrell equation for transient, semi-infinite diffusion:

$$I = \frac{nF\,A\,C_i\sqrt{D}}{\sqrt{\pi t}} \tag{11}$$

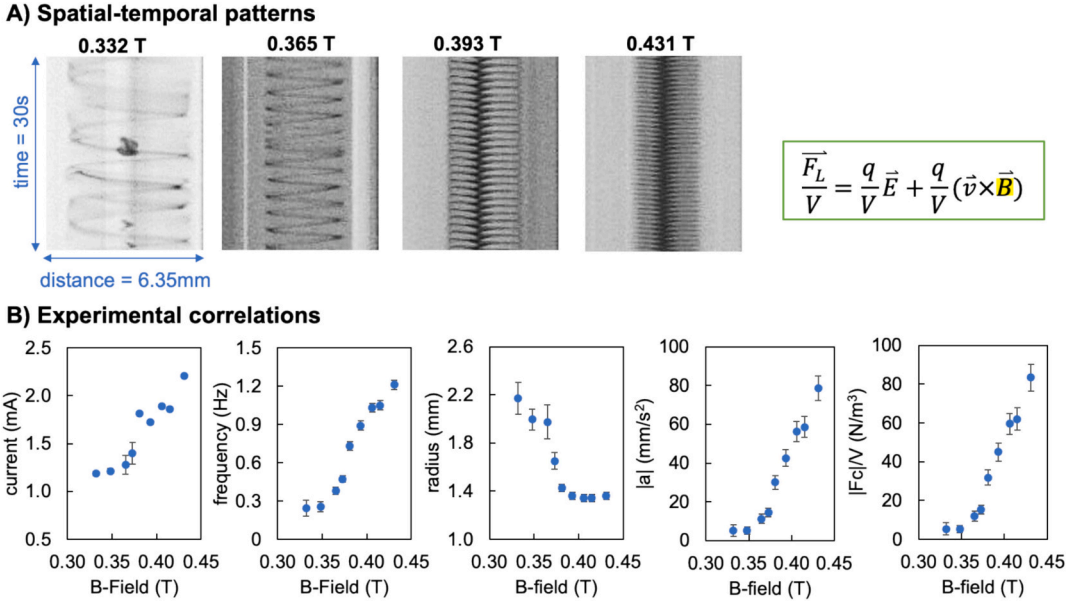

Fig. 3. The effect of magnetic field strength on Lorentz-induced fluidic motions. A) Selected spatio-temporal patterns showing changes in fluidic rotational radius and frequency as a function of magnetic field strength. B) Experimental quantification of the effect of B-field strength on current, fluidic rotational frequency, radii of rotation, centripetal acceleration ($|a| = 4\pi^2 r f^2$), and centripetal forces ($|F_C|/V = \rho|a|$). Note that 0.75 V (vs Ag/AgCl) was applied to the anode across all measurements. The strength of the magnetic field is controlled by changing the distance between the anode and the magnet, as characterized in Fig. S1.

Although Eq. (11) is not a quantitative model for the full study, it establishes the expected qualitative scaling of current with reactant concentration (C_i) and diffusion coefficient (D). Held at constant geometry, potential, and time (t), the term $\frac{nFA}{\sqrt{\pi t}}$ serves as a baseline constant for tracking trends—though electrode area (A) can be independently tuned (SI Sec. 5, Fig. S7). The following sections systematically vary C_i and D, noting that D scales inversely with fluidic viscosity (μ) via the Stokes-Einstein relation using an inert thickening agent.

2.3. The effect of reagent concentration

The chemical composition of electrochemical systems is diverse, often controllable, and plays a crucial role in experimental design and output. Many energy-related applications commonly utilize highly concentrated electrolytes. For example, water electrolysis typically uses 1 M KOH or 0.5 M H_2SO_4 solutions, and aqueous battery systems such as the Zn-MnO_2 battery routinely employ mixtures containing 1–2 M $ZnSO_4$ and 1 M $MnSO_4$ [34]. Alternatively, electroanalytical systems such as point-of-care diagnostics often deal with significantly more dilute samples [35]. To test how the concentration of the reactant influences $\vec{I}$ and components of the Lorentz force, we investigated the role of NaI concentration and quantified experimentally fluidic motions systematically. Based on the analysis of spatio-temporal patterns, we observe that, not only does the rate of rotation increase, but the induction period (amount of time between when a potential is applied to the system and the NaI_3 complex diffuses from the electrode surface) decreases as concentration increases. Fig. 4A-B shows that, with a constant B-field of 0.40 T applied to the system, an increase in concentration from 300 mM to 1000 mM results in a linear increase in $|\vec{I}|$, a near-linear increase in fluidic rotation frequency from 0.5 Hz to 1.4 Hz, and a non-linear decrease in radius from 1.5 mm to 1.2 mm. As a result, the centripetal acceleration increases non-linearly from ~20 mm/s^2 to ~90 mm/s^2.

The linear increase in current indicates that the production of net charges (q) increased as a function of concentration. The q term contributes to both the electric force component and the magnetic force component of Lorentz, which are two vectors pointing in different directions (Fig. S15). The plateauing of centripetal acceleration at high concentrations could be explained by the non-linear and angular contributions of these forces. The centripetal force as the net force in the horizontal plane is the sum of the Lorentz force and a fluidic drag force. Note that the drag force depends on viscosity, which will be discussed in the next section.

Practically, this framework may be limited at low analyte concentrations (<10 mM) where the proportional drop in ionic current renders the Lorentz force too weak to drive observable magneto-hydrodynamics. However, our model indicates that applying correspondingly higher $\vec{E}$ or $\vec{B}$ could theoretically recover these macroscopic Lorentz effects even in highly dilute regimes. Furthermore, the scaling behavior of our system—where current increases with concentration or magnetic field strength—aligns with foundational hydrodynamic models like those proposed by Willner et al. [36] While our experimental correlations mirror their theoretical predictions, a critical distinction exists: classical models assume the Lorentz force is equal to its magnetic force component ($\vec{F_L} = \vec{F_m}$), treating the bulk electric force component as zero ($\vec{F_E} = 0$). Our framework explicitly proves that $\vec{F_E}$ is non-zero and essential for quantifying force vectors and accurately predicting Lorentz effects.

2.4. The effect of fluidic viscosity

Although most electrochemical reactions are performed in aqueous media, certain applications (e.g., electrosynthesis or synthetic organic electrochemistry [37]) commonly utilize organic or mixed aqueous/organic electrolytes. These systems, as with aqueous systems containing ionic liquids can have significantly different viscosities compared to aqueous electrolytes composed of inorganic supporting electrolytes (e.g., KCl, H_2SO_4, KOH, etc.). Furthermore, gel electrolytes – which have a drastically higher viscosity than their liquid counterparts – are being investigated with many electrochemical systems/devices [38]. For

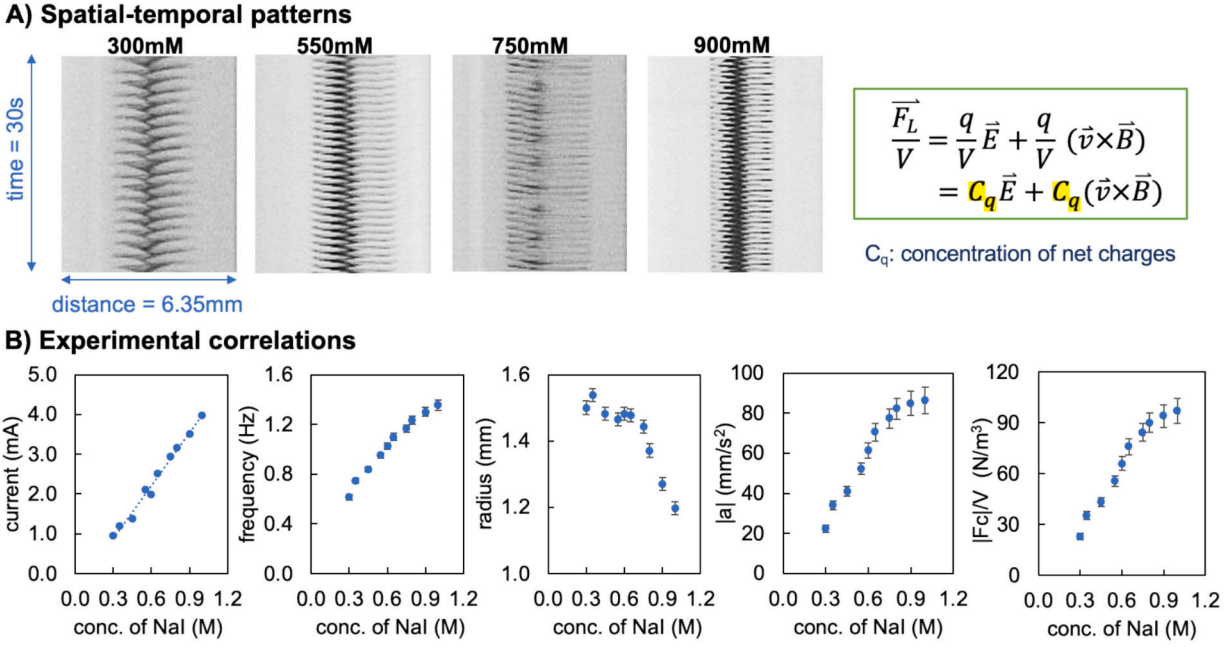

Fig. 4. The effect of the concentration of reactants (e.g., NaI) on Lorentz-induced fluidic motions. Mathematically, the net charged density is linearly proportional to the concentration of net charges, considering a unit volume that is much smaller than the electrochemical cell and these values are non-zero. A) Spatio-temporal patterns showing changes in fluidic rotational radius and frequency as a function of concentration. B) Quantifying the effect of reactant concentration on current, fluidic rotational frequencies and radii, centripetal acceleration, and centripetal forces. Across all measurements, 0.75 V (vs Ag/AgCl) was applied to the anode, and B = 0.40 T was measured at the anode surface.

example, gel electrolytes have been incorporated into flexible supercapacitors, batteries and dye-sensitized solar cells.

To evaluate the influence of viscosity on the observed magneto-hydrodynamic behavior, we varied the concentration of carboxylmethyl cellulose sodium salt (CMC) as the thickening agent added to an aqueous NaI solution (500 mM) to tune the viscosity of the medium without significant changes to its ion conductivity. Rheology measurements show that the resulting electrolytes are Newtonian fluids, meaning the viscosity of each electrolyte remains constant at different shear rates. Fig. 5A shows strong linear correlations between the viscosity and the concentration of added CMC (from 0 to 0.23 wt%). Fig. 5B-C shows that, as the viscosity of the medium increases from 0.9 to 1.6 mPa·s, fluidic rotational frequency decreases from 0.9 Hz to 0.7 Hz. Fluidic rotational radius changes only when the viscosity of the electrolytic solution is sufficiently viscous (e.g., above 1.5 mPa·s). Centripetal acceleration for this set of experiments ranges from 40 mm/s^2 (0.9 mPa·s) to 14 mm/s^2 (at 1.6 mPa·s), as shown in Fig. 5C. As the viscosity of the electrolytic medium increases, fluidic drag forces (F_d) increase (Fig. 5B), which are in the opposite direction of fluidic motion (SI, Fig. S15). Higher viscosity therefore slows down fluidic motion, in addition to reducing the ionic current and reducing the Lorentz force. The effect of viscosity is an important consideration for applying Lorentz forces to systems that use different types of electrolytes, as well as for systems that operate under different or fluctuating temperatures, as temperature can influence viscosity, in addition to chemical reactivity.

In addition to the effect of viscosity on F_d, viscosity (μ) is inversely correlated to diffusion coefficient (D) based on the Stokes-Einstein equation below:

$$D = \frac{k_B T}{6\pi R_0 \mu} \tag{12}$$

where R_0 is the solute radius, k_B is the Boltzmann constant, and T is the temperature (in K). When approximating $\frac{k_B T}{6\pi R_0}$ to a constant value across the set of experiments shown in Fig. 5, as viscosity increases, the diffusion coefficient of ions decreases, causing a decrease in current (Fig. 5C left, consistent with the Cottrell Eq. (11)). Such a decrease in ionic velocity decreases the F_m component of the Lorentz force, in addition to increasing F_d.

2.5. Analysis of forces

The periodic fluidic rotations observed in this study are governed by a net centripetal force. To simplify the analysis of forces, we analyzed forces near the electrode surface in the r-θ plane (SI Fig. S15). In a simplified force diagram, the net centripetal force is pointing radially inwards towards the anode, which is the sum of $\vec{F_E}$ (pointing radially outwards from the anode), $\vec{F_m}$ (initially perpendicular to the electric force, but gradually changes direction as v changes, until it reaches a steady state), and $\vec{F_d}$ (in the opposite direction of $\vec{v}$). The $\vec{F_E}$ component can then be calculated from a combination of experimental measurements and simulations, including rheological measurements of $\vec{F_d}$ (SI Sec. 10.3), electrochemically measured $\vec{J}$, simulated directions of $\vec{E}$ (SI Sec. 10.4, Fig. S18–19), the strength of $\vec{B}$, and experimentally measured angle between the $\vec{F_E}$ and $\vec{v}$ (SI Sec. 10.5 and Fig. S20). These calculations lead to an empirical $\frac{\vec{F_E}}{V}$ determined to be in the range of 10^1–10^2 N/m^3. Parameters that influence any of these force components are important to take into consideration when implementing Lorentz forces in electrochemical applications.

Additionally, we performed finite element analysis using COMSOL Multiphysics software to simulate Lorentz effects on fluidic motions qualitatively (driven by changes in trajectories of charged species) as a function of electric field strength and magnetic field strength. Fig. 6A shows trajectories of charged particles (in the horizontal r-θ plane) under the influence of a magnetic field (pointing vertically up in the z-direction and uniform across the horizontal r-θ plane; when the north side of the magnet is facing up) and an electric field based on dimensions of our experimental setup. Simulation results show rotational trajectories that are clockwise around the anode, and counter-clockwise around the cathode, in the opposite direction compared to when the south side of the magnet is facing up (Fig. 1c). The charged particle density appears higher closer to the electrodes than away from the electrodes and the particles speed is higher between the two electrodes than in the surrounding area, likely due to higher $\vec{E}$ and higher $\vec{J}$ in the inner region at a given radial distance. 2D maps of Lorentz forces

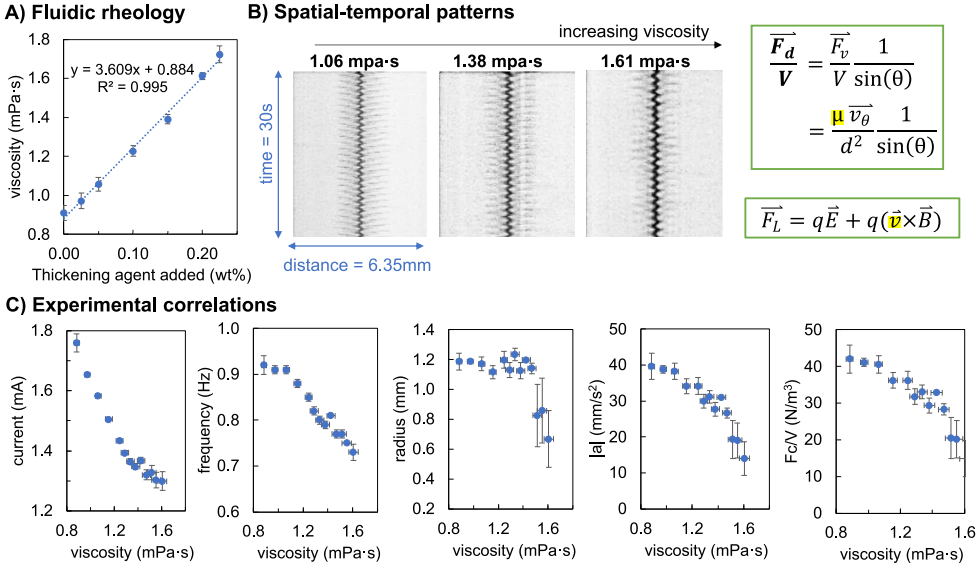

Fig. 5. The effect of fluidic viscosity on Lorentz-induced fluidic motions. A) Experimentally measured viscosity of NaI (500 mM) solution as a function of the concentration of carboxyl methylcellulose sodium salt (CMC) added as a thickening agent. B) Spatio-temporal patterns of selected experiments. C) Quantifying the effect of viscosity on current, fluidic rotational frequencies and radii, centripetal acceleration, and centripetal forces. Note that the change of electrolyte conductivity and density (with 500 mM NaI) is negligible with the addition of CMC (from 0 to 0.23 wt%). Across all measurements, 0.75 V (vs Ag/AgCl) was applied to the anode, and B = 0.40 T was measured at the anode surface.

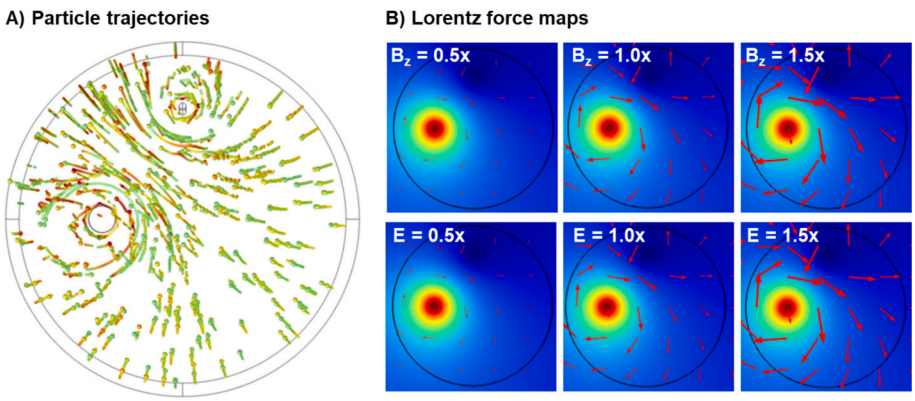

Fig. 6. Simulation snapshots (top view, in the r-θ plane) qualitatively show how an electric field coupled with a magnetic field can drive Lorentz-induced fluidic motions. A) A particle tracing module coupled with finite element analysis (using COMSOL Multiphysics) shows trajectories of charged particles under Lorentz effects. The color of particles qualitatively reflects their relative speed, with red being higher and blue/green being lower. B) 2D maps of Lorentz forces as a function of B-field strength $|\boldsymbol{B}|$ (0.5×, 1.0×, and 1.5×) and *E*-field strength $|\boldsymbol{E}|$ (0.5×, 1.0×, and 1.5×), assuming the current density is linearly proportional to the voltage applied. The size of red arrows represents the magnitude of Lorentz forces (on a logarithmic scale), while the color map indicates relative voltage. Force directions are simulated based on when the North-side of the magnet is facing upwards (i.e., magnetic field lines going out of the page).

(Fig. 6B) show that, when the strength of either the magnetic field or the ionic current increases, the magnitude of resulting Lorentz forces will increase. Results from simulation are qualitatively consistent with our experimental observations in the model system. The ability to correlate experimental and computational results in this simple system provides a predictive capability in future embodiments of magneto-electrochemical technologies.

3. Discussion

Lorentz forces significantly alter the trajectory of moving (net-charged) ionic species across the entire system, with impacts beyond interfacial processes and also in the electrolyte medium at a distance away from the electrode surface. In our model system, we observe that fluidic rotation increases the diffusion-limited electrochemical current through increased fluidic convection. Moreover, the frequency of fluidic rotation in the bulk matches the frequency of current oscillations (SI, Fig. S6), aligning bulk phenomena with surface processes, which could lead to innovative control mechanisms to alter surface processes on electrocatalysts.

Research in the field of magneto-electrochemistry has largely focused on application-based studies as opposed to fundamental interrogations, which is likely due to challenges quantifying the influence of diverse electrochemical parameters on experimental outputs (e.g., local vs. bulk fluidic rotation and observed current). Previously, visualization of fluidic rotation has relied on the introduction of beads, nanoparticles or dyes coupled with video analysis to gain insights into the resulting fluid dynamics of magneto-hydrodynamic systems. Our approach, which does not require any additives, simply utilizes the electrochemical oxidation product of iodide salts (e.g., triiodide complexes) as an in-situ generated fluidic tracer for the construction of spatio-temporal plots. These spatio-temporal plots not only simplify analysis but also provide a means of interrogating various experimental conditions and correlating rotational frequency (and radii) to current responses.

For energy-efficient mass transport, Lorentz-driven convection offers distinct advantages over a conventional rotating disk electrode (RDE). While an RDE drives fluid convection and thins the diffusion layer via direct mechanical rotation [39–41], our system non-mechanically enhances mass transport to yield current increases up to 100%. Thermodynamic calculations (SI Sec. 10.6) show that this induced hydrodynamics consumes less than 1% of the reaction's total electrochemical energy supply. However, unlike a mechanical RDE which can be driven to arbitrarily high rotation rates, the convective ceiling of a magneto-electrochemical system is governed by a coupled, multi-parameter space balancing $\vec{J}$, $\vec{E}$, and $\vec{B}$. Rather than being rigidly bounded by maximum attainable magnetic field strengths, our quantitative framework provides the predictive correlations needed to map and maximize this transport ceiling within a given reactor design. This non-contact approach lowers capital and operating costs while eliminating moving parts, offering a reliable alternative for compact, enclosed systems like batteries and fuel cells [33,42].

Another implication of this work for chemical engineering is the experimental confirmation that the electric field in solution (i.e., the ohmic potential drop) can be tuned to control convection. Reported experimental methods for measuring electric field and charge densities in electrochemical systems include electric force microscopy [43], electro-absorption spectroscopy [44], and Raman spectroscopy [45]. To date, most of the literature has focused on short (<10 μm) distances next to the electrode surface and reported rapid depletion of electric potential and ion density to negligible (or not measurable) values beyond these distances. Our experimentally obtained non-negligible effects of $\vec{F}_E$ (with $\frac{\vec{F}_E}{V}$ quantified to be on the order of 10^1–10^2 N/m^3 in our system) and visualized Lorentz effects extend well into the bulk electrolyte (millimeters to centimeters away from the electrode; Video S1). This suggests that reactor geometry (which defines the electric field topology) can be designed in tandem with magnetic field placement to induce convective mixing, offering a new dimension for electrochemical reactor design.

The framework presented in this paper has the potential for broad utility throughout chemical and chemical engineering applications. Precise control over fluidic motion can be particularly useful in diffusion-limited reactions such as the oxygen reduction reaction (ORR) which is plagued by low O_2 solubility and sluggish transport, or the electrochemical reduction of CO_2 which suffers from solubility and diffusivity issues, or the nitrate reduction reaction which also is significantly mass-transfer limited in remediation applications and NH_3 electrosynthesis. Moreover, energy storage devices such as aqueous-batteries [33], non-aqueous batteries (e.g., lithium ion [46]), regenerative fuel cells [42] and bio-electrochemical systems [47,48] all suffer from mass-transport limitations which could benefit from controlled Lorentz-force induced fluidic rotations. While our macro-scale cell geometry was designed as an analytical tool to decouple individual force components, this fundamental framework can be extended to predict Lorentz effects in these alternative configurations. For instance, in short-gap parallel architectures (e.g., sandwiched batteries), high local current densities lower the operational magnetic field threshold required to

actively suppress localized current anomalies and homogenize mass transfer. Low temperature or cryogenic systems, which suffer slow diffusion, could benefit from the enhanced mass-transport afforded by Lorentz effects. Additionally, our insights can help improve electrocatalysis for chemical production, such as chlor-alkali reactions [49] in industrial settings, and in growing fields of electro-organic synthesis [37] with early work on organic redox reactions in concentrated solutions [50,51].

4. Conclusions

This work establishes the first quantitative design framework for controlling solution-phase mass transport in electrochemical systems using the Lorentz force. By systematically deconstructing the interplay between key chemical parameters (reactant concentration, viscosity) and physical parameters (applied potential, magnetic field strength), we have transformed the Lorentz effect from a qualitative phenomenon into a predictive, quantitative tool. Our tracer-free analysis reveals a key design principle: the electric field (and its induced $\vec{F_E}$), often treated solely as a migration drive, interacts with the magnetic field (and its induced $\vec{F_m}$) to create controllable transport effects extending millimeters to centimeters from the electrode. This quantitative control over iodide redox chemistry—a reaction important in its own right for applications like dye-sensitized solar cells [52]—provides the foundation for engineering a wide range of electrochemical processes.

The design framework established here is broadly applicable to general electrochemical systems (including electrolytic cells, galvanic cells, or rechargeable batteries). It provides a rational pathway for engineering fluid dynamics in applications previously limited by diffusion. For example, in energy storage, this non-mechanical control of fluid motion could be used to suppress dendrite formation in lithium batteries [53,54], and promoting interfacial homogeneity and cyclability. In electro-organic synthesis [37,50,51], electrocatalysis [11,55], and bioelectrochemical systems (such as enzymatic biofuel cells) [47,48], it offers a low-energy method to enhance mass transport, improve yields, and potentially tune selectivity by controlling the residence time of intermediates at the electrode surface. This quantitative understanding will also advance the precision of electrochemical deposition and materials synthesis [56,57].

This framework now provides a clear path for exploring a rich, multiparameter design space; future work can leverage the interplay between chemical composition, electrode geometry, and magnetic field topology to achieve precise spatio-temporal control of reaction environments. It is important to translate these millimeter-scale transport phenomena into pilot-scale electrochemical reactor designs and optimize magnetic field topologies for continuous-flow systems. This quantitative control over ionic motion in solution bridges the gap between physical understanding of magnetism, experimental chemistry, and device engineering, enabling the design of next-generation technologies, such as ionic motors and transport systems, that can be complementary to today's electron-based devices.

CRediT authorship contribution statement

Haihui Joy Jiang: Writing – review & editing, Writing – original draft, Visualization, Validation, Supervision, Software, Project administration, Methodology, Investigation, Formal analysis, Data curation, Conceptualization. **Lais C. Brazaca:** Writing – review & editing, Visualization, Validation, Supervision, Software, Methodology, Investigation, Formal analysis, Data curation. **Thomas C. Underwood:** Writing – review & editing, Software, Methodology, Investigation, Formal analysis. **Ekaterina V. Skorb:** Visualization, Methodology, Investigation, Data curation, Conceptualization. **Mohamed K. Abd El-Rahman:** Visualization, Validation, Methodology, Investigation. **Craig A. Mascarenhas:** Writing – review & editing, Validation, Software, Formal analysis. **William T. McLeod:** Visualization, Validation, Investigation, Data curation. **Gigi Ni:** Visualization, Validation, Formal analysis, Data curation. **Brian Medrano:** Visualization, Validation, Formal analysis, Data curation. **Lukas Emge:** Methodology, Investigation, Formal analysis, Data curation. **Lee Belding:** Visualization, Methodology, Investigation, Data curation. **Albert S.Y. Wong:** Visualization, Software, Methodology, Formal analysis. **David M. Wilmouth:** Writing – review & editing. **Dimitar D. Sasselov:** Writing – review & editing. **James G. Anderson:** Writing – review & editing, Supervision. **Jeffrey G. Bell:** Writing – review & editing, Writing – original draft, Visualization, Validation, Supervision, Resources, Project administration, Methodology, Investigation, Funding acquisition, Formal analysis, Data curation, Conceptualization. **George M. Whitesides:** Writing – review & editing, Visualization, Supervision, Resources, Project administration, Methodology, Funding acquisition, Conceptualization.

Declaration of competing interest

Harvard University has filed a patent application PCT/US2023/35411.

The authors declare that they have no known competing financial interests or personal relationships that could have appeared to influence the work reported in this paper.

Acknowledgements

This work was supported by a grant from the Simons Foundation (290364FY21, GMW). Early work on this project was supported by the Department of Energy (award DE-FG02-00ER45852). GN and LE acknowledge summer research scholarships awarded by the Harvard Origin of Life Initiative. The authors acknowledge the use of shared facilities at the Center for Nanoscale Systems (CNS) supported by the Harvard MRSEC NSF award DMR-2011754. We thank Dr. Nicholas S. Colella at Harvard CNS for instrument support. JGB and WTM acknowledge support from the Washington Research Foundation (award number AWD005255). JGB also acknowledges support from the National Science Foundation under Grant No. 2501275. ASYW is supported by funding from the Netherlands Organisation for Scientific Research (NWO, Rubicon program, project no. 019.172EN.017). LCB acknowledges FAPESP for the financial support (Project number 2023/10141-2).

Appendix A. Supplementary data

Supplementary data to this article can be found online at https://doi.org/10.1016/j.cej.2026.178373.

Data availability

Data will be made available on request.

References

[1] Z.J. Oliver, D.J. Abrams, L. Cardinale, C.-J. Chen, G.L. Beutner, S. Caille, B. Cohen, L. Deng, M. Diwan, M.O. Frederick, K. Harper, J.M. Hawkins, D. Lehnherr, C. Lucky, A. Meyer, S. Noh, D. Nunez, K. Quasdorf, J. Teli, S.S. Stahl, M. Schreier, Scaling organic electrosynthesis: the crucial interplay between mechanism and mass transport, ACS Cent. Sci. 11 (4) (2025) 528–538.

[2] C. Heubner, M. Schneider, A. Michaelis, Diffusion-limited C-rate: a fundamental principle quantifying the intrinsic limits of Li-ion batteries, Adv. Energy Mater. 10 (2) (2020) 1902523.

[3] P. Dunne, J.M.D. Coey, Influence of a magnetic field on the electrochemical double layer, J. Phys. Chem. C 123 (39) (2019) 24181–24192.

[4] L.M. Monzon, J.M.D. Coey, Magnetic fields in electrochemistry: the Lorentz force. A mini-review, Electrochem. Commun. 42 (2014) 38–41.

[5] G. Hinds, F.E. Spada, J.M.D. Coey, T.R. Ní Mhíocháin, M.E.G. Lyons, Magnetic field effects on copper electrolysis, J. Phys. Chem. B 105 (39) (2001) 9487–9502.

[6] C. Liu, W. He, G. Xu, P. Zhang, M. Ni, Z. Sun, Magnetic field regulation of zinc dendrite growth in aqueous zinc batteries: a phase-field study, J. Energy Storage 146 (2026) 119836.

[7] K. Shen, X. Xu, Y. Tang, Recent progress of magnetic field application in lithium-based batteries, Nano Energy 92 (2022) 106703.
[8] H. Ko, W. Kim, M. Kang, S. Park, N. Kim, Y.C. Park, B. Kang, Effects of directional magnetic field on the performance and degradation of lithium-ion batteries, J. Energy Storage 153 (2026) 120867.
[9] W.T. McLeod, K.A. McCracken, P. Sireesha, N.H. Hille, J.G. Bell, Improving capacity retention of anode-free zinc batteries with simple geometry and Lorentz forces, ACS Appl. Mater. Interfaces 17 (28) (2025) 40546–40554.
[10] M.-Y. Lin, L.-W. Hourng, C.-W. Kuo, The effect of magnetic force on hydrogen production efficiency in water electrolysis, Int. J. Hydrog. Energy 37 (2) (2012) 1311–1320.
[11] M.S. Kodaimati, R. Gao, S.E. Root, G.M. Whitesides, Magnetic fields enhance mass transport during electrocatalytic reduction of CO2, Chem. Catal. 2 (4) (2022) 797–815.
[12] G. Ibáñez, S. Cuevas, M.L. de Haro, Optimization analysis of an alternate magnetohydrodynamic generator, Energy Convers. Manag. 43 (14) (2002) 1757–1771.
[13] S.-H. Park, C.-W. Lee, Lorentz force-type integrated motor-bearing system in dual rotor disk configuration, IEEE/ASME Trans. Mechatron. 10 (6) (2005) 618–625.
[14] H. Wen, J. Shah, R.S. Balaban, Hall effect imaging, IEEE Trans. Biomed. Eng. 45 (1) (1998) 119–124.
[15] M.C. Weston, M.D. Gerner, I. Fritsch, Magnetic fields for fluid motion, Anal. Chem. 82 (9) (2010) 3411–3418.
[16] K.M. Grant, J.W. Hemmert, H.S. White, Magnetic field-controlled microfluidic transport, J. Am. Chem. Soc. 124 (3) (2002) 462–467.
[17] S.Z. Luo, K. Elouarzaki, Z.C.J. Xu, Electrochemistry in magnetic fields, Angew. Chem.-Int. Ed. 61 (27) (2022).
[18] A. Fiala, L.C. Pitchford, J.P. Boeuf, Two-dimensional, hybrid model of low-pressure glow discharges, Phys. Rev. E 49 (6) (1994) 5607–5622.
[19] S. Kolev, A. Bogaerts, A 2D model for a gliding arc discharge, Plasma Sources Sci. Technol. 24 (1) (2015) 015025.
[20] P. Vensaus, Y. Liang, J.-P. Ansermet, G.J.A.A. Soler-Illia, M. Lingenfelder, Enhancement of electrocatalysis through magnetic field effects on mass transport, Nat. Commun. 15 (1) (2024) 2867.
[21] Y. Zhang, C. Liang, J. Wu, H. Liu, B. Zhang, Z. Jiang, S. Li, P. Xu, Recent advances in magnetic field-enhanced electrocatalysis, ACS Appl. Energy Mater. 3 (11) (2020) 10303–10316.
[22] S.K.A. Raj, C.S. Rout, Recent developments, challenges and future prospects of magnetic field effects in supercapacitors, J. Mater. Chem. A 11 (11) (2023) 5495–5519.
[23] H.H. Bau, Applications of magneto electrochemistry and magnetohydrodynamics in microfluidics, Magnetochemistry 8 (11) (2022).
[24] G. Salinas, C. Lozon, A. Kuhn, Unconventional applications of the magnetohydrodynamic effect in electrochemical systems, Curr. Opin. Electrochem. 38 (2023) 101220.
[25] J.M.D. Coey, G. Hinds, Magnetic electrodeposition, J. Alloys Compd. 326 (1) (2001) 238–245.
[26] I. Uechi, M. Fujiwara, Y. Fujiwara, Y. Yamamoto, Y. Tanimoto, Magnetic field effects on anodic oxidation of potassium iodide, Bull. Chem. Soc. Jpn. 75 (11) (2002) 2379–2382.
[27] J.D. Newson, A.C. Riddiford, The kinetics of the iodine redox process at platinum electrodes, J. Electrochem. Soc. 108 (7) (1961) 699.
[28] L.M. Dané, L.J.J. Janssen, J.G. Hoogland, The iodine/iodide redox couple at a platinum electrode, Electrochim. Acta 13 (3) (1968) 507–518.
[29] S.R. Ragsdale, H.S. White, Imaging microscopic magnetohydrodynamic flows, Anal. Chem. 71 (10) (1999) 1923–1927.
[30] V. Gatard, J. Deseure, M. Chatenet, Use of magnetic fields in electrochemistry: a selected review, Curr. Opin. Electrochem. 23 (2020) 96–105.
[31] L. Elias, A. Chitharanjan Hegde, Effect of magnetic field on HER of water electrolysis on Ni–W alloy, Electrocatalysis 8 (4) (2017) 375–382.
[32] C. Hunt, Z. Zhang, K. Ocean, R.P. Jansonius, M. Abbas, D.J. Dvorak, A. Kurimoto, E.W. Lees, S. Ghosh, A. Turkiewicz, F.A. Garcés Pineda, D.K. Fork, C. P. Berlinguette, Quantification of the effect of an external magnetic field on water oxidation with cobalt oxide anodes, J. Am. Chem. Soc. 144 (2) (2022) 733–739.
[33] A. Sheelam, D.L. Glasco, J.G. Bell, Retaining the reversible capacity by Lorentz forces for enhanced cyclability of aqueous zinc-bromide batteries using internal magnets, Chem. Eng. J. 461 (2023) 141900.
[34] X. Zheng, K. Xu, Y. Ma, J. Sun, B. Han, R. Luo, M. Wang, N. Chen, L. Song, Q. Zhao, W. Chen, Development of durable Zn–MnO2 battery via a functionalized hydrogel film, Adv. Energy Mater. 14 (25) (2024) 2400038.
[35] A. Nemiroski, D.C. Christodouleas, J.W. Hennek, A.A. Kumar, E.J. Maxwell, M. T. Fernández-Abedul, G.M. Whitesides, Universal mobile electrochemical detector designed for use in resource-limited applications, Proc. Natl. Acad. Sci. 111 (33) (2014) 11984–11989.
[36] O. Lioubashevski, E. Katz, I. Willner, Magnetic field effects on electrochemical processes: a theoretical hydrodynamic model, J. Phys. Chem. B 108 (18) (2004) 5778–5784.
[37] E.J. Horn, B.R. Rosen, P.S. Baran, Synthetic organic electrochemistry: an enabling and innately sustainable method, ACS Central Sci. 2 (5) (2016) 302–308.
[38] X. Cheng, J. Pan, Y. Zhao, M. Liao, H. Peng, Gel polymer electrolytes for electrochemical energy storage, Adv. Energy Mater. 8 (7) (2018) 1702184.
[39] A.J. Bard, L.R. Faulkner, J. Leddy, C.G. Zoski, Electrochemical Methods: Fundamentals and Applications Vol. 2, Wiley New York, 1980.
[40] S. Bruckenstein, B. Miller, Unraveling reactions with rotating electrodes, Acc. Chem. Res. 10 (2) (1977) 54–61.
[41] R.F. Probstein, Physicochemical Hydrodynamics: An Introduction, John Wiley & Sons, 2005.
[42] A. Shahzad, H.J. Jiang, K.-F. Aguey-Zinsou, Unitized regenerative fuel cells: fundamental challenges and advancements, Renew. Sust. Energ. Rev. 215 (2025) 115631.
[43] J.D. Slinker, J.A. DeFranco, M.J. Jaquith, W.R. Silveira, Y.-W. Zhong, J.M. Moran-Mirabal, H.G. Craighead, H.D. Abruña, J.A. Marohn, G.G. Malliaras, Direct measurement of the electric-field distribution in a light-emitting electrochemical cell, Nat. Mater. 6 (11) (2007) 894–899.
[44] J.C. deMello, J.J.M. Halls, S.C. Graham, N. Tessler, R.H. Friend, Electric field distribution in polymer light-emitting electrochemical cells, Phys. Rev. Lett. 85 (2) (2000) 421–424.
[45] H. Shi, B. Zhao, J. Ma, M.J. Bronson Jr., Z. Cai, J. Chen, Y. Wang, M. Cronin, L. Jensen, S.B. Cronin, Measuring local electric fields and local charge densities at electrode surfaces using graphene-enhanced Raman spectroscopy (GERS)-based stark-shifts, ACS Appl. Mater. Interfaces 11 (39) (2019) 36252–36258.
[46] M.S. Hossain, L.I. Stephens, M. Hatami, M. Ghavidel, D. Chhin, J.I.G. Dawkins, L. Savignac, J. Mauzeroll, S.B. Schougaard, Effective mass transport properties in lithium battery electrodes, ACS Appl. Energy Mater. 3 (1) (2020) 440–446.
[47] E. Katz, O. Lioubashevski, I. Willner, Magnetic field effects on bioelectrocatalytic reactions of surface-confined enzyme systems: enhanced performance of biofuel cells, J. Am. Chem. Soc. 127 (11) (2005) 3979–3988.
[48] G. Salinas, T. Safarik, M. Meneghello, S. Bichon, S. Gounel, N. Mano, A. Kuhn, Magnetohydrodynamic enhancement of biofuel cell performance, Chem. Eur. J. 31 (9) (2025) e202403329.
[49] M. Hou, L. Chen, Z. Guo, X. Dong, Y. Wang, Y. Xia, A clean and membrane-free chlor-alkali process with decoupled Cl2 and H2/NaOH production, Nat. Commun. 9 (1) (2018) 438.
[50] J. Lee, X. Gao, L.D.A. Hardy, H.S. White, Influence of magnetic fields on the voltammetric response of microelectrodes in highly concentrated organic redox solutions, J. Electrochem. Soc. 142 (6) (1995) L90.
[51] S.R. Ragsdale, J. Lee, X. Gao, H.S. White, Magnetic field effects in electrochemistry. Voltammetric reduction of acetophenone at microdisk electrodes, J. Phys. Chem. 100 (14) (1996) 5913–5922.
[52] J.G. Rowley, B.H. Farnum, S. Ardo, G.J. Meyer, Iodide chemistry in dye-sensitized solar cells: making and breaking I–I bonds for solar energy conversion, J. Phys. Chem. Lett. 1 (20) (2010) 3132–3140.
[53] Y. Zhao, L. Wang, H.R. Byon, High-performance rechargeable lithium-iodine batteries using triiodide/iodide redox couples in an aqueous cathode, Nat. Commun. 4 (1) (2013) 1896.
[54] K. Shen, Z. Wang, X. Bi, Y. Ying, D. Zhang, C. Jin, G. Hou, H. Cao, L. Wu, G. Zheng, Y. Tang, X. Tao, J. Lu, Magnetic field–suppressed lithium dendrite growth for stable lithium-metal batteries, Adv. Energy Mater. 9 (20) (2019) 1900260.
[55] A. Sheelam, J.G. Bell, Uniform electrodeposition of Pd nanoparticles on MoS2-x nanosheets using magnetic fields for improved mass utilization in hydrogen evolution, Int. J. Hydrog. Energy 56 (2024) 348–357.
[56] J.M.D. Coey, G. Hinds, M.E.G. Lyons, Magnetic-field effects on fractal electrodeposits, Europhys. Lett. (EPL) 47 (2) (1999) 267–272.
[57] K. Kołodziejczyk, E. Mięko, M. Zieliński, M. Jaksender, D. Szczukocki, K. Czarny, B. Krawczyk, Influence of constant magnetic field on electrodeposition of metals, alloys, conductive polymers, and organic reactions, J. Solid State Electrochem. 22 (6) (2018) 1629–1647.